

Electronic properties of kagome metal ScV_6Sn_6 using high-field torque magnetometry

Keshav Shrestha^{1,*}, Binod Regmi^{2,*}, Ganesh Pokharel³, Seong-Gon Kim^{2,‡}, Stephen D. Wilson³, David E. Graf^{4,5}, Birendra A. Magar⁶, Cole Phillips¹, and Thanh Nguyen¹

¹Department of Chemistry and Physics, West Texas A&M University, Canyon, Texas 79016, USA


²Department of Physics and Astronomy, Mississippi State University, Mississippi State, Mississippi 39762, USA

³Materials Department, University of California, Santa Barbara, California 93106, USA

⁴Department of Physics, Florida State University, Tallahassee, Florida 32306, USA

⁵National High Magnetic Field Laboratory, Tallahassee, Florida 32310, USA

⁶Department of Physics, New Mexico State University, Las Cruces, New Mexico 88003, USA

 (Received 29 March 2023; revised 13 November 2023; accepted 14 November 2023; published 7 December 2023)

This work presents electronic properties of the kagome metal ScV_6Sn_6 using de Haas–van Alphen (dHvA) oscillations and density-functional theory (DFT) calculations. The torque signal with the applied fields up to 43 T shows clear dHvA oscillations with six major frequencies, five of them are below 400 T (low frequencies) and one is nearly 2800 T (high frequency). The Berry phase calculated using the Landau level fan diagram near the quantum limit is approximately π , which suggests the nontrivial band topology in ScV_6Sn_6 . To explain the experimental data, we computed the electronic band structure and Fermi surface using DFT in both the pristine and charge-density wave (CDW) phases. Our results confirm that the CDW phase is energetically favorable, and the Fermi surface undergoes a severe reconstruction in the CDW state. Furthermore, the angular dependence of the dHvA frequencies are consistent with the DFT calculations. The detailed electronic properties presented here are invaluable for understanding the electronic structure and CDW order in ScV_6Sn_6 , as well as in other vanadium-based kagome systems.

DOI: [10.1103/PhysRevB.108.245119](https://doi.org/10.1103/PhysRevB.108.245119)

Kagome materials have recently garnered enormous interest as they exhibit many interesting physical and material properties, such as charge-density wave (CDW), nontrivial topology, geometrically frustrated magnetism [1–3]. The atoms in kagome compounds form a quasi-2D lattice resembling Japanese basket-weaving patterns [4]. For example, a new vanadium-based family AV_3Sb_5 ($A = \text{K}, \text{Rb}, \text{and Cs}$) form a hexagonal lattice of V atoms that are coordinated by Sb atoms [5–7]. Numerous exotic quantum phenomena, superconductivity (SC) ($T_c \sim 0.3\text{--}3\text{ K}$), CDW order near $T_{\text{CDW}} \sim (80\text{--}110\text{ K})$, a van Hove singularity, etc., have been discovered in this family [8–11]. Recent quantum oscillations studies [12–22] on AV_3Sb_5 have verified the nontrivial band topology and also revealed a severe reconstruction of the Fermi surface in the CDW phase.

In a search for a new kagome system, a vanadium-based RV_6Sn_6 ($R = \text{Rare earth}$) (also called “166” compounds) [23–28] have been discovered. Among 166 compounds, GdV_6Sn_6 , HoV_6Sn_6 , and YV_6Sn_6 are already known to show topological features [25,29]. Arachchige *et al.* [30] recently reported ScV_6Sn_6 , which is the only compound in the 166 family exhibiting a CDW order below $T_{\text{CDW}} = 92\text{ K}$. The T_{CDW} transition is confirmed to be of the first-order nature [30,31]. However, no SC has been detected in ScV_6Sn_6 either

under ambient or high pressure conditions up to 11 GPa [32]. The x-ray and neutron-scattering experiments [30] reveal the $\sqrt{3} \times \sqrt{3} \times 3$ structural modulation in the CDW phase of ScV_6Sn_6 . A thorough understanding of the Fermi surface is crucial to comprehend the CDW phase in ScV_6Sn_6 . However, to date, there have been no reports on the electronic properties of ScV_6Sn_6 through quantum oscillations measurements.

In this work, we present electronic properties of ScV_6Sn_6 single crystal using torque magnetometry and density-functional theory (DFT) calculations. We could resolve six distinct frequencies in dHvA oscillations, five of them below 400 T and one is very high $\sim 2800\text{ T}$. The Berry phase computed at the quantum limit is approximately π , which provides evidence for the nontrivial topology of ScV_6Sn_6 . Moreover, our first-principles calculations in the CDW phase are consistent with experimental results.

High-quality single crystals of ScV_6Sn_6 were synthesized using the flux-based growth technique. The side and top views of the crystal structure of ScV_6Sn_6 are displayed in Fig. 1(a). The top view clearly shows the Kagome network of V atoms. Torque measurements were performed at the National High Magnetic Field Laboratory (NHMFL) in Tallahassee, Florida, using a hybrid magnet with dc magnetic fields up to 43 T. Electronic band structure and Fermi surface were calculated using spin-polarized DFT with projector-augmented wave (PAW) potentials as implemented in Vienna *ab initio* simulation package (VASP). The detailed sample synthesis and experimental details are presented in the Supplemental Material (SM) [33]. Our temperature-dependent

*These authors contributed equally to this work.

†Corresponding address: kshrestha@wtamu.edu

‡Corresponding address: sk162@msstate.edu

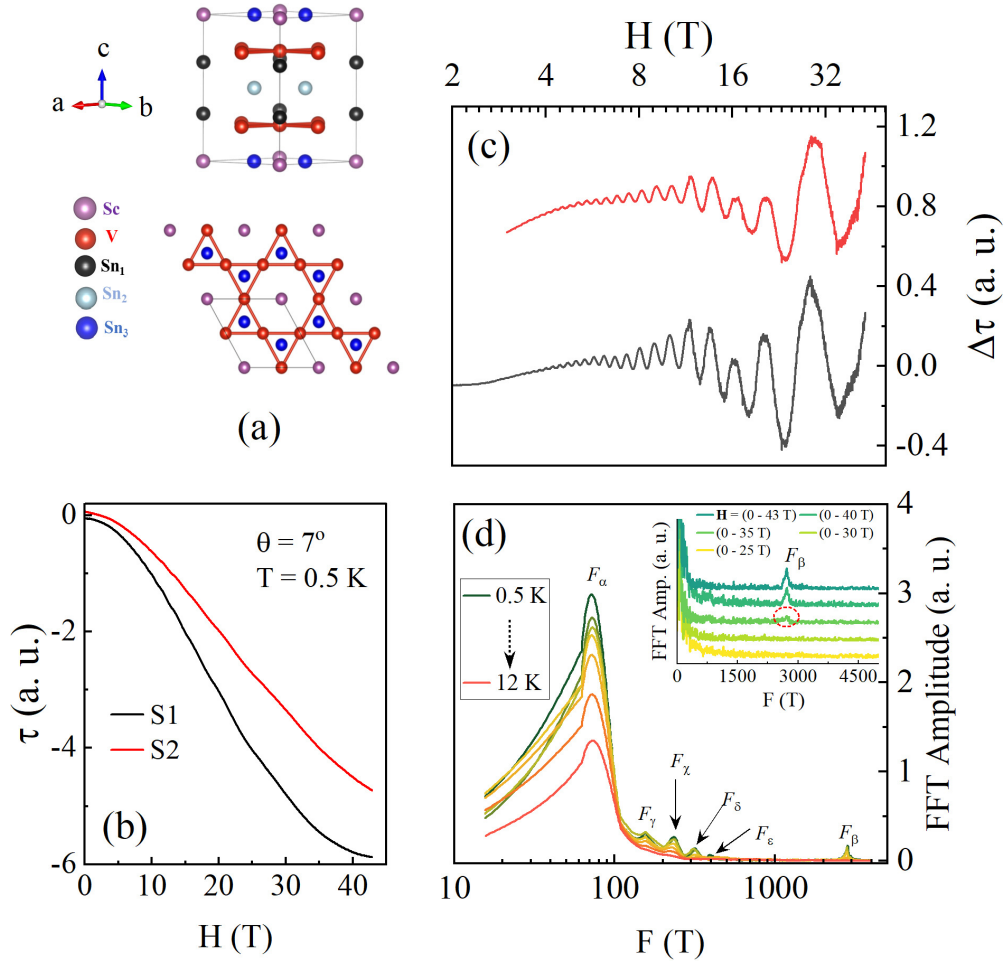


FIG. 1. (a) A unit cell (upper panel) and top view (bottom panel) of ScV₆Sn₆, showing the kagome network consists of V-atoms. (b) Magnetic torque τ of two ScV₆Sn₆ single crystals (S1 and S2) up to 43 T at $\theta = 7^\circ$ and $T = 0.5$ K. (c) Background-subtracted torque $\Delta\tau$ for data shown in (b). There are clear dHvA oscillations above 4 T. (d) The FFT spectra for S2 at different temperatures. Inset: The FFT spectra of dHvA oscillation data for different magnetic field ranges. F_β emerges above 35 T, as indicated by the dotted circle. The x axes in (c) and (d) are in log scales, and the data in inset (d) is shifted vertically for better visibility.

magnetic susceptibility data shows a sharp drop below 92 K due to the CDW transition that is consistent with recent reports [30,41,42] (Fig. S1 in SM [33]).

Figure 1(b) shows the magnetic torque τ for two ScV₆Sn₆ single crystals (S1 and S2) with applied fields H up to 43 T at 0.5 K. The τ signal decreases with H and shows indication of dHvA oscillations, which is clearly reflected in the background subtracted data in Fig. 1(c). The oscillations in both samples are evident and even start at relatively low magnetic fields of around 4 T. Moreover, the oscillations for both samples appear to be similar, and their frequency spectra are comparable as well (Fig. S2 in SM [33]).

The frequency spectra of S2 at different temperatures, obtained after performing the fast Fourier transform (FFT) of the background-subtracted quantum oscillations data, are presented in Fig. 1(d). There are six distinct frequency peaks, five of which are low frequencies ($F_\alpha = 77 \pm 12$ T, $F_\gamma = 155 \pm 8$ T, $F_\chi = 235 \pm 10$ T, $F_\delta = 314 \pm 15$ T, and $F_\epsilon = 394 \pm 18$ T) and the remaining one is high frequency $F_\beta = 2834 \pm 30$ T. At higher temperature, the amplitude of the frequencies decreases. This behavior can be explained

by the Lifshitz-Kosevich (LK) formula [43,44]. We used the LK formula to fit the temperature-dependent FFT data and estimated the effective masses of the charge carriers to be $m_\alpha^* = 0.19 m_e$ and $m_\beta^* = 0.77 m_e$, where m_e is the free electron mass, for α and β pockets, respectively (Fig. S3 in SM [33]). These m^* values are slightly higher than those observed in other 166 family compounds [45], but they are comparable to the values reported for AV₃Sb₅ [12,13,20–22].

The observation of high-frequency F_β in our data is very intriguing as it emerges only at high magnetic fields. To precisely determine the field value at which the high-frequency signal emerges, we randomly chose torque data at $\theta = 45^\circ$ and analyzed that data at different magnetic field ranges. Although the low-frequency signals are present at magnetic field ranges, the high-frequency signal emerges only above 35 T, as shown in Fig. 1(d). Therefore, it is interesting to understand Fermi surface topology of F_β by measuring dHvA oscillation at different tilt angles with respect to the applied field.

The angular dependence of quantum oscillations provides information about the shape, size, and dimensionality of the

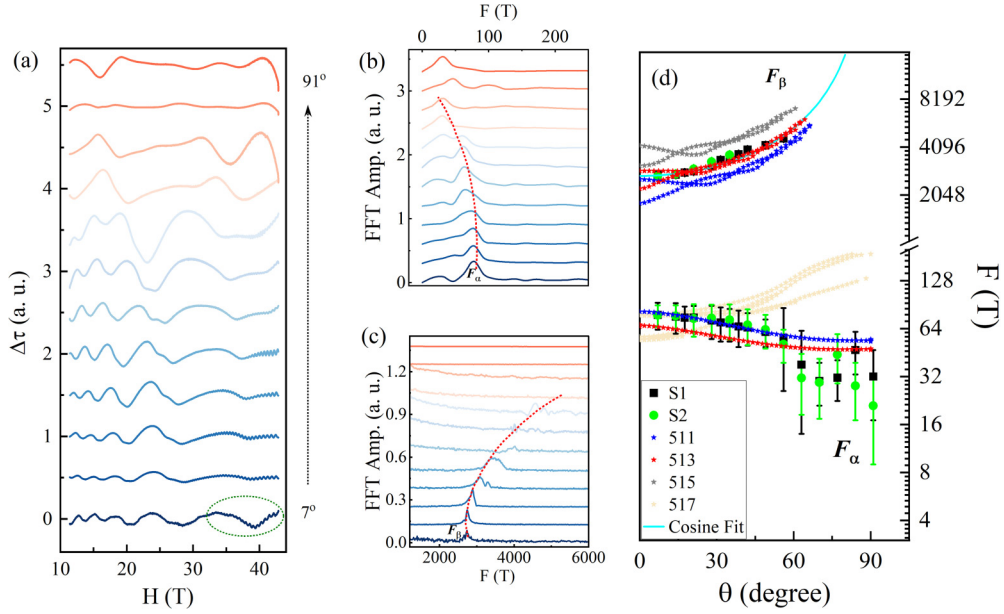


FIG. 2. (a) Torque data after subtracting smooth polynomial background ($\Delta\tau$) data for ScV_6Sn_6 at selected θ values. As highlighted by dotted ellipse at 7° , the high frequencies start emerging only at higher magnetic fields above 35 T. Angular dependence of dHva frequencies in the range of (b) -20 – 250 T and (c) 1200 – 6000 T. Both F_α and F_β shift while changing θ , as guided by the dotted curves. The curves in (a)–(c) are shifted vertically for clarity. Some of the curves in (a)–(b) have been divided or multiplied by factors to highlight the frequency trend. (d) Angular dependence of F_α and F_β for S1 (squares) and S2 (circles). F_α decreases at higher θ values and clearly resolved up to 91° , whereas F_β increases monotonically and disappears above 56° . The error bar for each frequency data point is determined as half the width at half maximum of the respective peak in the FFT spectrum. The solid curve represents the $1/\cos\theta$ behavior of F_β . Frequencies derived from the DFT calculations are shown as dotted lines. The Fermi level in the DFT calculations was shifted downward by 10 meV for a better comparison with the experiments.

Fermi surface [6,43,46,47]. To explore this, we conducted torque measurements at various tilt angles. In Fig. 2(a), the background-subtracted torque data for ScV_6Sn_6 is displayed at specific θ values. As shown in Figure 2(a), there are clearly more than two periods, representing multiple quantum oscillation frequencies. Notably, a shorter period emerges above 35 T, as indicated by the dashed ellipse, signaling the higher frequency F_β . This observation aligns with our frequency analysis data across different field ranges, as illustrated in Fig. 1(d) inset. Figures 2(b) and 2(c) represent the frequency spectra of data shown in 2(a) in the range of -20 – 250 T and 1200 – 6000 T, respectively. At higher θ values, F_α decreases, whereas F_β increases, as indicated by the dashed curves. F_β signal gets weaker at higher θ values and can be resolved only up to 56° .

Figure 2(d) shows the angular dependence of F_α and F_β for both S1 and S2. Frequencies derived from S1 and S2 are comparable to one another and show the same angular variation. As expected, F_α is observed at all θ values up to 91° , and it decreases at higher θ values. Whereas, F_β increases at higher θ values and it nearly follows $1/\cos\theta$ behavior as indicated by the solid curve. This suggests that the Fermi surface corresponding to F_β is nearly cylindrical [6,48,49]. Moreover, the disappearance of F_β above 56° further supports its cylindrical shape [6,50–52]. For comparison, we have included frequencies derived from DFT calculations. As seen in the graph, the angular variations of F_α and F_β are consistent with DFT results, which will be discussed in detail later. We observe that other frequencies (F_γ , F_χ , F_δ , and F_ϵ) exhibit a very weak

angular dependence similar to that of F_α , as illustrated in Fig. S4 in SM [33]. Their values are nearly integer multiples of F_α , suggesting that F_γ , F_χ , F_δ , and F_ϵ could potentially be higher harmonics of F_α . Conducting torque measurements at even higher fields (above 43 T) might provide a more precise determination of the angular dependence of F_χ , F_δ , and F_ϵ aiding in the identification of their origin.

The analysis of our angular-dependent quantum oscillations data reveals that ScV_6Sn_6 possesses both quasi-2D and 3D Fermi surfaces. To understand the topological property, we calculated the Berry phase Φ_B of the α band by constructing a Landau level (LL) fan diagram [6,43,51]. The Φ_B value is π (or zero) for a topologically nontrivial (or trivial) system [6,49,53]. The magnetic torque is given by $\vec{\tau} = V\mu_0\vec{M} \times \vec{H} = V\mu_0MH\sin\lambda$, where V , μ_0 , and λ represent the volume of the sample, the permeability of the free space, and the angle between M and H , respectively. Assuming $\lambda = 90^\circ$, the perpendicular component of the magnetization M_\perp with the external field can be determined from the torque data. Figure 3(a) shows the background-subtracted magnetization ΔM_\perp vs $1/H$ plot for ScV_6Sn_6 . Since there are multiple frequencies present in the data, we isolated oscillations for F_α using a FFT bandpass filter [21,22]. The gray and magenta curves in Fig. 3(a) are the raw and filtered data, respectively. In the extracted oscillations, there is a single frequency of 79 T, as indicated in the inset. The LL index for the minima and maxima positions were assigned as $(N - \frac{1}{4})$ and $(N + \frac{1}{4})$, respectively, while constructing the LL fan diagram [43,54–56].

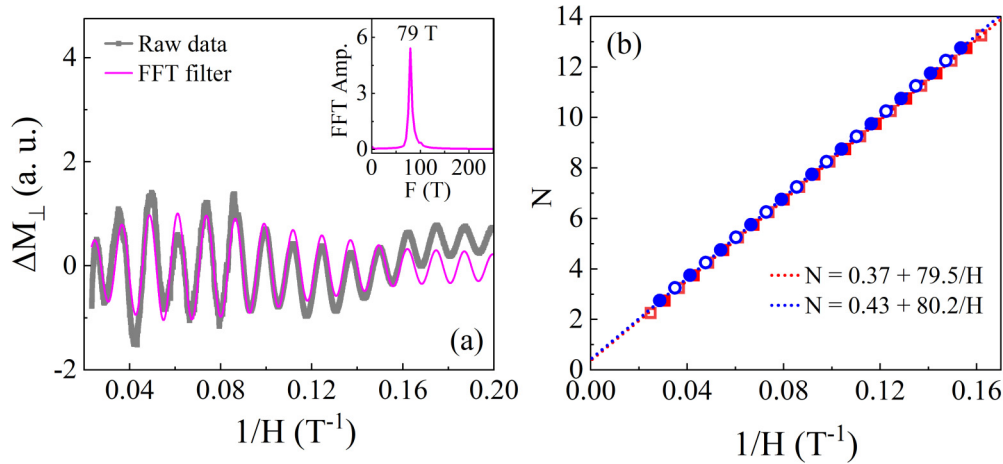


FIG. 3. Landau level (LL) fan diagram. (a) Separation of the dHvA oscillations corresponding to F_α using the band-pass filter of (70–100 T). The grey and magenta curves represent the raw and filtered data, respectively. Inset: FFT of the processed dHvA oscillations. A single FFT peak at 79 T confirms the presence of quantum oscillations only for F_α . (b) LL fan diagram for F_α for both S1 (squares) and S2 (circles). Minima (solid symbols) and maxima (open symbols) of oscillations were assigned to $(N - 1/4)$ and $(N + 1/4)$, respectively, for constructing the LL fan diagram. The dotted lines are linear extrapolations of data in the limit $1/H \rightarrow 0$.

The LL fan diagrams for S1 and S2 are depicted in Fig. 3(b). From the linear extrapolation of the LL fan diagram data in the limit $1/H \rightarrow 0$, we have obtained the intercept values, that is, $\Phi_B/2\pi = (0.43 \pm 0.01)$ and (0.37 ± 0.01) for S1 and S2, respectively. These numbers correspond to $\Phi_B \approx \pi$, implying the nontrivial topology of the α band. Based on the linear extrapolation, we have also obtained the slopes of (80.2 ± 1.2) T and (79.5 ± 1.6) T for S1 and S2, respectively. The slope values correspond closely to $F_\alpha = 79$ T, which provides confirmation that the linear extrapolation of the N vs $1/H$ data is precise in determining the intercept (and thus the Φ_B value), and that the band-pass filter retains the original dHvA oscillation signal without significant error. It is noteworthy that the use of high magnetic fields (43 T) causes the charge carriers to reach the second LL (near the quantum limit). Consequently, the Φ_B value obtained using the linear extrapolation is trustworthy and precise. Recently, S. Mizafari *et al.* [57] have also observed a large anomalous Hall signal, and C. Yi *et al.* [58], have reported nontrivial topology at a lower frequency of ~ 50 T using Shubnikov–de Haas oscillation measurements, which is consistent with our results.

In order to account for the experimental findings and understand the effect of the CDW order on Fermi surface, we conducted DFT calculations for both the pristine and CDW phases of ScV_6Sn_6 . Electronic bands of the pristine ScV_6Sn_6 with spin-orbit coupling (SOC), obtained from our first-principles calculations, are shown in Fig. 4(a). Similar to other 166 kagome materials [23,26,59], there exist two Dirac points near the Fermi level at the K point, as indicated by the dotted circles and a flat band (the gray shaded area). Here, the inclusion of SOC results in an opening of gaps at both Dirac points, while without SOC, there is no such gap present (Fig. S5 in SM [33]). The two bands, namely 57 and 59, crossing the Fermi level, are responsible for the formation of the Fermi surface of pristine ScV_6Sn_6 (see Fig. S6 in SM [33]). The Fermi surface exhibits more 3D FS character (band 57) containing necks in its belly, suggesting that the system is

strongly bonded along the out-of-plane direction, whereas the band 59 forms the small electron pockets near the Brillouin zone boundary. These Fermi surface sheets are consistent with previous study [31].

Recently, H. Arachchige *et al.* [30] carried out the x-ray and neutron-scattering experiments and reported the presence of $\sqrt{3} \times \sqrt{3} \times 3$ structural modulation in the CDW phase of ScV_6Sn_6 . Therefore, we conducted our investigation of the CDW phase using this specific configuration. Our DFT results suggest that the CDW phase is more energetically favorable than the pristine phase by 5.4 meV/unit cell, which is in close agreement with the previously reported value of 5.8 meV/unit cell [60]. We conducted further investigations on the impact of CDW and crystallographic distortion on the Fermi surface. We observed a substantial distortion (~ 0.2 Å) of the Sc and Sn_1 atoms along the c axis, as illustrated in Fig. S7 in SM [33]. This lattice distortion results in a significant reconstruction of electronic bands and Fermi surface sheets.

The folded electronic band structure of ScV_6Sn_6 in the CDW phase is displayed in Fig. S8 in SM [33]. Due to the large number of atoms and consequently electrons, as well as the CDW-distorted structure, analyzing the effect of the CDW in the folded band structure is challenging. Therefore, we performed band unfolding, as presented in Fig. 4(b). As expected, all features observed in the pristine phase are also preserved in the CDW state, too. There are additional band features, especially along Γ -A direction, which is associated with the structural distortion in the CDW phase. This effective band structure is consistent with the previous studies [61]. Figure 4(c) shows the Fermi surfaces of ScV_6Sn_6 in the CDW phase. The Fermi surfaces are composed of contributions from four bands, namely 511, 513, 515, and 517. The Fermi surfaces of bands 511, 513, and 515 resemble 2D cylinders containing hole pockets, while that for band 517 forms small electron pockets near the Brillouin zone boundary. Additionally, all of these Fermi surfaces feature small prismatic-shapelike pockets at the center.

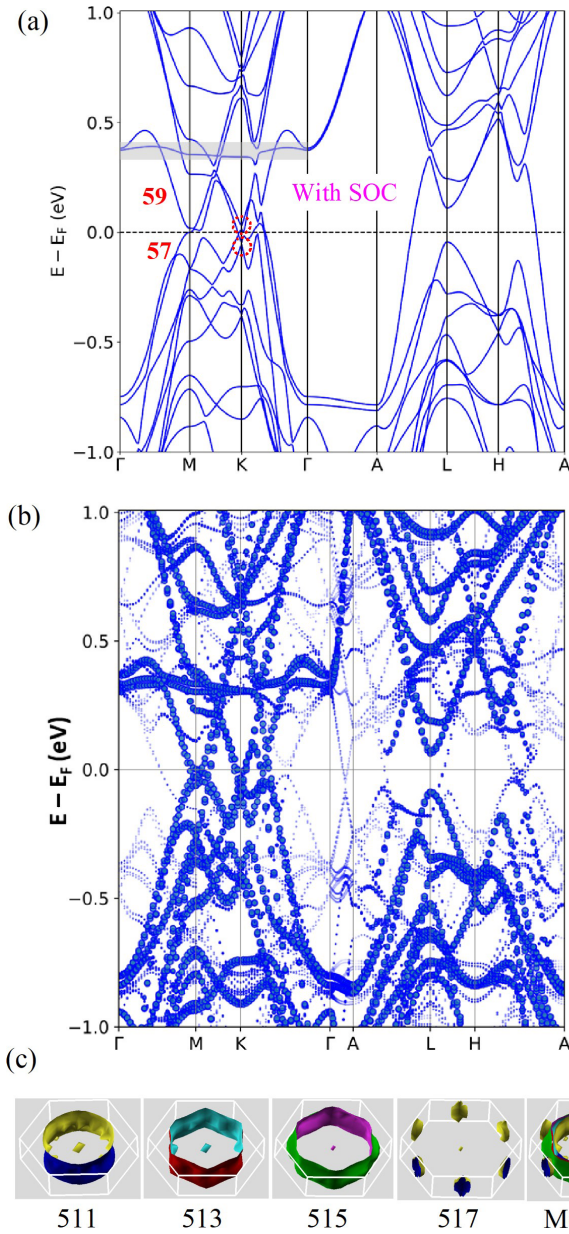


FIG. 4. Band structure and Fermi surface. (a) Electronic band structure of pristine ScV_6Sn_6 with SOC. The flat band is denoted by the gray area, and the Dirac points near the Fermi level at the K point are indicated by dotted circles. (b) Unfolded band structure in the $\sqrt{3} \times \sqrt{3} \times 3$ CDW phase of ScV_6Sn_6 . Bands of higher weight correspond to bands from the pristine state. The pristine band features are preserved in the CDW state. (c) Band-resolved Fermi surfaces of ScV_6Sn_6 in the $\sqrt{3} \times \sqrt{3} \times 3$ CDW phase with SOC included.

To explore the lattice instability, we calculated the phonon spectrum of ScV_6Sn_6 in both the pristine and CDW phases, as presented in Fig. 5. Our phonon spectrum is consistent with previously reported data [60]. In the pristine phase, the phonon dispersion exhibits imaginary phonon modes, particularly along the A - L - H direction. This observation indicates dynamic instability within that region of the Brillouin zone, suggesting potential structural distortions or phase transitions in the material. Conversely, the absence of imaginary

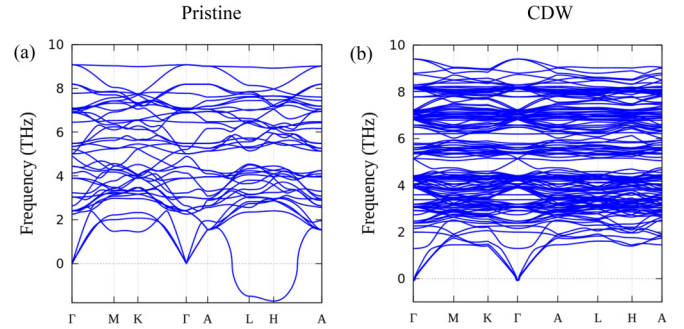


FIG. 5. (a) Phonon spectrum of ScV_6Sn_6 in the (a) pristine and (b) $\sqrt{3} \times \sqrt{3} \times 3$ CDW phase. The imaginary phonon frequency in the pristine phase implies the lattice instability along A - L - H direction of the Brillouin zone.

frequencies in the CDW phase confirms the dynamical stability of the $\sqrt{3} \times \sqrt{3} \times 3$ CDW phase. Furthermore, our calculations of the density of states (DOS) in the pristine phase (Fig. S9 in SM [33]) indicate that the electronic states are dominated by vanadium d orbitals near the Fermi level. However, we observe only a limited reduction in DOS at the Fermi level in the CDW phase. This is because the CDW distortion mainly arises from the significant vertical displacement (~ 0.2 Å) of Sc and Sn_1 , not from the nominal in-plane movement of vanadium, also observed recently in Ref. [62]. However, its effect on DOS is trivial since Sc and Sn provide a nominal contribution to the DOS as shown in plot S9(a) in SM [33]. Our DOS results are consistent with recent studies [63] on ScV_6Sn_6 .

To compare with the experimental data, we measured the area of each energy isosurface forming the Fermi surface and then computed the oscillatory frequencies using the Onsager relation [64]. We employed the SKEAF code to compute all potential frequencies derived from each electronic band contributing to the formation of the Fermi surface in ScV_6Sn_6 . The calculated angular dependence of frequencies from different bands is plotted in Fig. 2(d) together with experimental data. As observed in the figure, while frequencies derived from both bands 511 and 513 describe the behavior of F_α , band 511 provides a better match in terms of the value of F_α . This implies that F_α originates from the prismatic-shapelike pocket of the Fermi surface of band 511. We notice that F_α deviates slightly above 60° . This could be due to the fact that at higher tilt angles, the dHvA oscillations get weaker, and frequency peaks are not as well defined as at lower angles. The frequencies coming from all three bands, 511, 513, and 515, exhibit an upward trend with increasing θ , similar to that of F_β . Among these frequencies, F_β aligns with the one derived from band 513, confirming its origin from the outer cylindrical shape of the Fermi surface in band 513. Nearly $1/\cos\theta$ behavior of F_β further confirms its origin from the cylindrical-shapelike Fermi surface. As seen in Fig. 2(d), the frequency of band 517 is ~ 60 T at 0° and increases at higher θ values. However, we have not observed any corresponding frequency peak from this band in the experiment. Furthermore, we shifted the Fermi level downward by 10 meV during DFT calculations. This adjustment, though *ad hoc*, accounts for the doping

effect, considering the ambiguity in the experimental Fermi level [54,65].

To summarize, we investigated the Fermiology of ScV₆Sn₆ using torque magnetometry and DFT calculations. Our findings reveal clear dHvA oscillations in the torque signal, with six distinct frequencies, five of which are below 400 T and one frequency near 2800 T. The use of NHMFL's high-field facility up to 43 T is crucial for calculating the Berry phase near the quantum limit and determining the nontrivial topological feature of ScV₆Sn₆. Additionally, this high field enables the observation of the high-frequency signal near 2800 T, which appears only above 35 T of the applied field. For further investigation, we also carried out the electronic band structure, Fermi surface, and phonon calculations in both pristine and CDW phases using DFT. There exist two Dirac points near the Fermi level at the K point and a flat band along Γ -M-K- Γ direction. The Fermi surface undergoes a severe reconstruction in the CDW phase and four bands contribute to the Fermi surface. We found that the $\sqrt{3} \times \sqrt{3} \times 3$

CDW phase in ScV₆Sn₆ is energetically favorable, and our phonon calculations confirm its stability. Angular dependence of dHvA oscillations is consistent with those calculated by the DFT calculations. The detailed electronic properties of ScV₆Sn₆ presented in this study are novel and crucial for understanding the CDW order and nontrivial topology not only in ScV₆Sn₆ but also in other vanadium-based kagome families.

The work at the West Texas A&M University is supported by the Killgore Faculty Research program, the KRC Undergraduate and Graduate Student Research Grants, and the Welch Foundation (Grant No. AE-0025). G.P. and S.W.D. gratefully acknowledge support via the UC Santa Barbara NSF Quantum Foundry funded via the Q-AMASE-i program under Award No. DMR-1906325. A portion of this work was performed at the National High Magnetic Field Laboratory, which is supported by National Science Foundation Cooperative Agreement No. DMR-2128556 and the State of Florida.

-
- [1] L. Ye, M. Kang, J. Liu, F. von Cube, C. R. Wicker, T. Suzuki, C. Jozwiak, A. Bostwick, E. Rotenberg, D. C. Bell, L. Fu, R. Comin, and J. G. Checkelsky, *Nature (London)* **555**, 638 (2018).
- [2] J.-X. Yin, W. Ma, T. A. Cochran, X. Xu, S. S. Zhang, H.-J. Tien, N. Shumiya, G. Cheng, K. Jiang, B. Lian *et al.*, *Nature (London)* **583**, 533 (2020).
- [3] K. Jiang, T. Wu, J.-X. Yin, Z. Wang, M. Z. Hasan, S. D. Wilson, X. Chen, and J. Hu, *Natl. Sci. Rev.* **10**, nwac199 (2022).
- [4] M. Mekata, *Phys. Today* **56**, 12 (2003).
- [5] B. R. Ortiz, L. C. Gomes, J. R. Morey, M. Winiarski, M. Bordelon, J. S. Mangum, I. W. H. Oswald, J. A. Rodriguez-Rivera, J. R. Neilson, S. D. Wilson, E. Ertekin, T. M. McQueen, and E. S. Toberer, *Phys. Rev. Mater.* **3**, 094407 (2019).
- [6] B. R. Ortiz, P. M. Sarte, E. M. Kenney, M. J. Graf, S. M. L. Teicher, R. Seshadri, and S. D. Wilson, *Phys. Rev. Mater.* **5**, 034801 (2021).
- [7] B. R. Ortiz, S. M. L. Teicher, Y. Hu, J. L. Zuo, P. M. Sarte, E. C. Schueller, A. M. Milinda Abeykoon, M. J. Krogstad, S. Rosenkranz, R. Osborn, R. Seshadri, L. Balents, J. He, and S. D. Wilson, *Phys. Rev. Lett.* **125**, 247002 (2020).
- [8] F. H. Yu, D. H. Ma, W. Z. Zhuo, S. Q. Liu, X. K. Wen, B. Lei, J. J. Ying, and X. H. Chen, *Nat. Commun.* **12**, 3645 (2021).
- [9] K. Y. Chen, N. N. Wang, Q. W. Yin, Y. H. Gu, K. Jiang, Z. J. Tu, C. S. Gong, Y. Uwatoko, J. P. Sun, H. C. Lei, J. P. Hu, and J. G. Cheng, *Phys. Rev. Lett.* **126**, 247001 (2021).
- [10] N. N. Wang, K. Y. Chen, Q. W. Yin, Y. N. N. Ma, B. Y. Pan, X. Yang, X. Y. Ji, S. L. Wu, P. F. Shan, S. X. Xu, Z. J. Tu, C. S. Gong, G. T. Liu, G. Li, Y. Uwatoko, X. L. Dong, H. C. Lei, J. P. Sun, and J.-G. Cheng, *Phys. Rev. Res.* **3**, 043018 (2021).
- [11] M. Kang, S. Fang, J.-K. Kim, B. R. Ortiz, S. H. Ryu, J. Kim, J. Yoo, G. Sangiovanni, D. D. Sante, B.-G. Park, C. Jozwiak, A. Bostwick, E. Rotenberg, E. Kaxiras, S. D. Wilson, J.-H. Park, and R. Comin, *Nat. Phys.* **18**, 301 (2022).
- [12] F. H. Yu, T. Wu, Z. Y. Wang, B. Lei, W. Z. Zhuo, J. J. Ying, and X. H. Chen, *Phys. Rev. B* **104**, L041103 (2021).
- [13] Q. Yin, Z. Tu, C. Gong, Y. Fu, S. Yan, and H. Lei, *Chin. Phys. Lett.* **38**, 037403 (2021).
- [14] S.-Y. Yang, Y. Wang, B. R. Ortiz, D. Liu, J. Gayles, E. Derunova, R. Gonzalez-Hernandez, L. Ľmejkal, Y. Chen, S. S. P. Parkin, S. D. Wilson, E. S. Toberer, and T. M. M. N. Ali, *Sci. Adv.* **6**, eabb6003 (2020).
- [15] K. Nakayama, Y. Li, T. Kato, M. Liu, Z. Wang, T. Takahashi, Y. Yao, and T. Sato, *Phys. Rev. X* **12**, 011001 (2022).
- [16] B. R. Ortiz, S. M. L. Teicher, L. Kautzsch, P. M. Sarte, N. Ratcliff, J. Harter, J. P. C. Ruff, R. Seshadri, and S. D. Wilson, *Phys. Rev. X* **11**, 041030 (2021).
- [17] H. Luo, Q. Gao, H. Liu, Y. Gu, D. Wu, C. Yi, J. Jia, S. Wu, X. Luo, Y. Xu *et al.*, *Nat. Commun.* **13**, 273 (2022).
- [18] Y. Fu, N. Zhao, Z. Chen, Q. Yin, Z. Tu, C. Gong, C. Xi, X. Zhu, Y. Sun, K. Liu, and H. Lei, *Phys. Rev. Lett.* **127**, 207002 (2021).
- [19] W. Zhang, L. Wang, C. W. Tsang, X. Liu, J. Xie, W. C. Yu, K. T. Lai, and S. K. Goh, *Phys. Rev. B* **106**, 195103 (2022).
- [20] C. Broyles, D. Graf, H. Yang, X. Dong, H. Gao, and S. Ran, *Phys. Rev. Lett.* **129**, 157001 (2022).
- [21] K. Shrestha, M. Shi, T. Nguyen, D. Miertschin, K. Fan, L. Deng, D. E. Graf, X. Chen, and C.-W. Chu, *Phys. Rev. B* **107**, 075120 (2023).
- [22] K. Shrestha, R. Chapai, B. K. Pokharel, D. Miertschin, T. Nguyen, X. Zhou, D. Y. Chung, M. G. Kanatzidis, J. F. Mitchell, U. Welp, D. Popović, D. E. Graf, B. Lorenz, and W. K. Kwok, *Phys. Rev. B* **105**, 024508 (2022).
- [23] G. Pokharel, S. M. L. Teicher, B. R. Ortiz, P. M. Sarte, G. Wu, S. Peng, J. He, R. Seshadri, and S. D. Wilson, *Phys. Rev. B* **104**, 235139 (2021).
- [24] J. Lee and E. Mun, *Phys. Rev. Mater.* **6**, 083401 (2022).
- [25] S. Peng, Y. Han, G. Pokharel, J. Shen, Z. Li, M. Hashimoto, D. Lu, B. R. Ortiz, Y. Luo, H. Li, M. Guo, B. Wang, S. Cui, Z. Sun, Z. Qiao, S. D. Wilson, and J. He, *Phys. Rev. Lett.* **127**, 266401 (2021).
- [26] E. Rosenberg, J. M. DeStefano, Y. Guo, J. S. Oh, M. Hashimoto, D. Lu, R. J. Birgeneau, Y. Lee, L. Ke, M. Yi, and J.-H. Chu, *Phys. Rev. B* **106**, 115139 (2022).

- [27] X. Zhang, Z. Liu, Q. Cui, Q. Guo, N. Wang, L. Shi, H. Zhang, W. Wang, X. Dong, J. Sun, Z. Dun, and J. Cheng, *Phys. Rev. Mater.* **6**, 105001 (2022).
- [28] G. Pokharel, B. Ortiz, J. Chamorro, P. Sarte, L. Kautzsch, G. Wu, J. Ruff, and S. D. Wilson, *Phys. Rev. Mater.* **6**, 104202 (2022).
- [29] Y. Hu, X. Wu, Y. Yang, S. Gao, N. C. Plumb, A. P. Schnyder, W. Xie, J. Ma, and M. Shi, *Sci. Adv.* **8**, eadd2024 (2022).
- [30] Hasitha W. Suriya Arachchige, W. R. Meier, M. Marshall, T. Matsuoka, R. Xue, M. A. McGuire, R. P. Hermann, H. Cao, and D. Mandrus, *Phys. Rev. Lett.* **129**, 216402 (2022).
- [31] T. Hu, H. Pi, S. Xu, L. Yue, Q. Wu, Q. Liu, S. Zhang, R. Li, X. Zhou, J. Yuan, D. Wu, T. Dong, H. Weng, and N. Wang, *Phys. Rev. B* **107**, 165119 (2023).
- [32] X. Zhang, J. Hou, W. Xia, Z. Xu, P. Yang, A. Wang, Z. Liu, J. Shen, H. Zhang, X. Dong, Y. Uwatoko, J. Sun, B. Wang, Y. Guo, and J. Cheng, *Materials* **15**, 7372 (2022).
- [33] See Supplemental Material at <http://link.aps.org/supplemental/10.1103/PhysRevB.108.245119> for the detail information, which include Refs. [34–40].
- [34] G. Kresse and J. Furthmüller, *Phys. Rev. B* **54**, 11169 (1996).
- [35] G. Kresse and D. Joubert, *Phys. Rev. B* **59**, 1758 (1999).
- [36] W. Kohn and L. J. Sham, *Phys. Rev.* **140**, A1133 (1965).
- [37] J. P. Perdew, K. Burke, and M. Ernzerhof, *Phys. Rev. Lett.* **77**, 3865 (1996).
- [38] A. Kokalj, *Journal of Molecular Graphics and Modelling* **17**, 176 (1999).
- [39] P. Rourke and S. Julian, *Comput. Phys. Commun.* **183**, 324 (2012).
- [40] A. Togo and I. Tanaka, *Scr. Mater.* **108**, 1 (2015).
- [41] M. Tuniz, A. Consiglio, D. Puntel, C. Bigi, S. Enzner, G. Pokharel, P. Orgiani, W. Bronsch, F. Parmigiani, V. Polewczyk, P. D. C. King, J. W. Wells, I. Zeljkovic, P. Carrara, G. Rossi, J. Fujii, I. Vobornik, S. D. Wilson, R. Thomale, T. Wehling, G. Sangiovanni, G. Panaccione, F. Cilento, D. D. Sante, and F. Mazzola, (2023), [arXiv:2302.10699](https://arxiv.org/abs/2302.10699).
- [42] S. Cheng, Z. Ren, H. Li, J. Oh, H. Tan, G. Pokharel, J. M. DeStefano, E. Rosenberg, Y. Guo, Y. Zhang, Z. Yue, Y. Lee, S. Gorovikov, M. Zonno, M. Hashimoto, D. Lu, L. Ke, F. Mazzola, J. Kono, R. J. Birgeneau, J.-H. Chu, S. D. Wilson, Z. Wang, B. Yan, M. Yi, and I. Zeljkovic, (2023), [arXiv:2302.12227](https://arxiv.org/abs/2302.12227).
- [43] D. Shoenberg, *Magnetic Oscillations in Metals* (Cambridge University Press, 1984).
- [44] K. Shrestha, V. Marinova, D. Graf, B. Lorenz, and C. Chu, *J. Appl. Phys.* **122**, 145901 (2017).
- [45] W. Ma, X. Xu, J.-X. Yin, H. Yang, H. Zhou, Z.-J. Cheng, Y. Huang, Z. Qu, F. Wang, M. Z. Hasan, and S. Jia, *Phys. Rev. Lett.* **126**, 246602 (2021).
- [46] K. Shrestha, V. Marinova, D. Graf, B. Lorenz, and C. W. Chu, *Phys. Rev. B* **95**, 075102 (2017).
- [47] K. Shrestha, V. Marinova, D. Graf, B. Lorenz, and C. W. Chu, *J. Appl. Phys.* **122**, 125901 (2017).
- [48] A. A. Taskin and Y. Ando, *Phys. Rev. B* **84**, 035301 (2011).
- [49] K. Shrestha, V. Marinova, B. Lorenz, and C. W. Chu, *J. Phys.: Condens. Matter* **30**, 185601 (2018).
- [50] K. Shrestha, V. Marinova, B. Lorenz, and P. C. W. Chu, *Phys. Rev. B* **90**, 241111(R) (2014).
- [51] K. Shrestha, D. E. Graf, V. Marinova, B. Lorenz, and P. C. Chu, *Philos. Mag.* **97**, 1740 (2017).
- [52] J. G. Analytis, R. D. McDonald, S. C. Riggs, J.-H. Chu, G. S. Boebinger, and I. R. Fisher, *Nat. Phys.* **6**, 960 (2010).
- [53] K. Shrestha, *Magnetotransport Studies on Topological Insulators* (2015).
- [54] T. Nguyen, N. Aryal, B. K. Pokharel, L. Harnagea, D. Mierstchin, D. Popović, D. E. Graf, and K. Shrestha, *Phys. Rev. B* **106**, 075154 (2022).
- [55] K. Shrestha, M. Shi, B. Regmi, T. Nguyen, D. Miertschin, K. Fan, L. Z. Deng, N. Aryal, S.-G. Kim, D. E. Graf, X. Chen, and C. W. Chu, *Phys. Rev. B* **107**, 155128 (2023).
- [56] K. Shrestha, D. Miertschin, R. Sankar, B. Lorenz, and C. W. Chu, *J. Phys.: Condens. Matter* **33**, 335501 (2021).
- [57] S. Mozaffari, W. R. Meier, R. P. Madhugaria, N. Peshchenko, S.-H. Kang, J. W. Villanova, H. W. S. Arachchige, G. Zheng, Y. Zhu, K.-W. Chen, K. Jenkins, D. Zhang, A. Chan, L. Li, M. Yoon, Y. Zhang, and D. G. Mandrus, (2023), [arXiv:2305.02393](https://arxiv.org/abs/2305.02393) [cond-mat.str-el].
- [58] C. Yi, X. Feng, P. Yanda, S. Roychowdhury, C. Felser, and C. Shekhar, Charge density wave induced anomalous Hall effect in kagome ScV₆Sn₆ (2023), [arXiv:2305.04683](https://arxiv.org/abs/2305.04683) [cond-mat.mtrl-sci].
- [59] S.-H. Kang, H. Li, W. R. Meier, J. W. Villanova, S. Hus, H. Jeon, H. W. S. Arachchige, Q. Lu, Z. Gai, J. Denlinger, R. Moore, M. Yoon, and D. Mandrus, [arXiv:2302.14041](https://arxiv.org/abs/2302.14041) (2023).
- [60] H. Tan and B. Yan, *Phys. Rev. Lett.* **130**, 266402 (2023).
- [61] H. Hu, Y. Jiang, D. Călugăru, X. Feng, D. Subires, M. G. Vergniory, C. Felser, S. Blanco-Canosa, and B. A. Bernevig, (2023), [arXiv:2305.15469](https://arxiv.org/abs/2305.15469) [cond-mat.str-el].
- [62] G. Pokharel, B. R. Ortiz, L. Kautzsch, S. J. G. Alvarado, K. Mallayya, G. Wu, E.-A. Kim, J. P. C. Ruff, S. Sarker, and S. D. Wilson, *Phys. Rev. Mater.* **7**, 104201 (2023).
- [63] S. Cao, C. Xu, H. Fukui, T. Manjo, M. Shi, Y. Liu, C. Cao, and Y. Song, Competing charge-density wave instabilities in the kagome metal ScV₆Sn₆ (2023), [arXiv:2304.08197](https://arxiv.org/abs/2304.08197) [cond-mat.str-el].
- [64] According to the Onsager's relation, the quantum oscillation measured frequency of an electron orbit (F) which is perpendicular to the applied magnetic field is related to the area of the Fermi surface (A) by $F = \frac{\phi_0}{2\pi^2} A$ where $\phi_0 = 2.07 \times 10^{-15}$ Tm₂ is the quantum of flux.
- [65] W. Zheng, R. Schönemann, S. Mozaffari, Y.-C. Chiu, Z. B. Goraum, N. Aryal, E. Manousakis, T. M. Siegrist, K. Wei, and L. Balicas, Bulk Fermi surfaces of the Dirac type-ii semimetallic candidate NiTe₂, *Phys. Rev. B* **102**, 125103 (2020).